Low-Threshold Topological Pumping in Toroidal Spin-1 Bose–Einstein Condensate

Xue-Ying Yang(杨雪滢)[1†], Peng Liu(刘鹏)[1†], Hui-Bo Hong(洪辉博)[1], Si-Lin Chen(陈思霖)[2], Juan Li(李娟)[1], and Rui-Fang Dong(董瑞芳)[1,3*]

[1]*Key Laboratory of Time Reference and Applications, National Time Service Center, Chinese Academy of Sciences, Xi'an 710600, China*
[2]*Shaanxi Key Laboratory for Theoretical Physics Frontiers, Institute of Modern Physics, Northwest University, Xi'an 710127, China*
[3]*School of Astronomy and Space Science, University of Chinese Academy of Sciences, Beijing 100049, China*

(Received 2 February 2026; accepted manuscript online 3 March 2026)

Singular spin-nematic vortices are unique topological excitations in spin-orbit-coupled spin-1 Bose–Einstein condensates. However, dynamically generating them in harmonic traps requires excessive Raman coupling to overcome the high energy cost of creating a density-depleted core. We demonstrate that a toroidal trapping potential naturally resolves this geometric mismatch. By accommodating the vortex core, the toroidal geometry lowers the formation threshold by $\sim 50\%$ and significantly broadens the stable phase boundary. Crucially, this geometry-assisted stabilization enables deterministic topological pumping. Instead of the abrupt phase jumps observed in harmonic traps that completely bypass the singular vortex, the toroidal potential supports a clean, stepwise adiabatic evolution ($|L_z = 0\rangle \to |1\rangle \to |2\rangle$). Our results provide a robust, low-power protocol for initializing spin-nematic quantum qutrits, bridging the gap between theoretical prediction and experimental realization.

DOI: 10.1088/0256-307X/43/4/040302 CSTR: 32039.14.0256-307X.43.4.040302

1. Introduction. The experimental realization of synthetic spin–orbit coupling (SOC) in ultracold atomic gases has established a versatile platform for simulating topological phases of matter and gauge-field-induced phenomena.[1–5] Recently, research interest has shifted from static phase diagram mapping to non-equilibrium dynamics and nonlinear excitations,[6–9] as well as atomtronic quantum devices.[10,11] In contrast to spin-1/2 systems, spin-1 spin–orbit coupled Bose–Einstein condensates (BECs) possess an extended symmetry group that supports complex tensor magnetic orders and novel stripe supersolids.[12–17] These rich internal degrees of freedom host unique topological defects—specifically, the exotic spin-nematic vortex.[18–23] Characterized by a central phase singularity and a quantized winding number (L_z), this state embodies the intrinsic locking between spin texture and superfluid circulation. Physically, such exotic vortices are not only key topological excitations within the spinor phase diagram but also serve as ideal models for investigating non-Abelian statistics.[24–26] Consequently, establishing a deterministic dynamical protocol to manipulate these modes is a crucial step toward utilizing such systems for topological quantum information processing.

Although the static phase diagram of spin-1 spin–orbit coupled BEC is well-established,[27–29] dynamical realization remains challenging. In harmonic traps, the system is prone to roton instabilities, which complicate the dynamical passage through phase boundaries.[30,31] A more fundamental obstacle is the geometric incompatibility between the trapping potential and the target state: the $L_z = 1$ vortex requires a density-depleted core, which incurs a high energetic cost at the trap center where density is maximized.[32,33] Consequently, this energetic mismatch suppresses the intermediate exotic vortex, inducing a direct level crossing between the trivial and double-vortex phases ($L_z : 0 \to 2$) that bypasses the target state completely.[34,35] Furthermore, heating from Raman lasers limits the experimental lifetime and prevents slow parameter sweeps required for adiabatic evolution.[36] Therefore, high-fidelity preparation requires moving beyond interaction control to directly engineering the trap geometry.[37,38]

In this Letter, we propose using a toroidal trap to overcome these geometric limitations. The ring geometry significantly broadens the stability region of the exotic spin-nematic vortex, allowing it to exist at much lower Raman coupling strengths. Quantitatively, increasing the central barrier height lowers the formation threshold by approximately 50%, which minimizes heating risks and enhances experimental feasibility. Crucially, the toroidal geometry

†These authors contributed equally to this work.
*Corresponding author. Email: dongruifang@ntsc.ac.cn
© 2026 Chinese Physical Society and IOP Publishing Ltd. All rights, including for text and data mining, AI training, and similar technologies, are reserved.

enables deterministic topological pumping. Unlike the random jumps observed in harmonic traps, the ring potential recovers a clean, stepwise evolution ($L_z : 0 \to 1 \to 2$). Our results provide a robust, geometry-assisted protocol for realizing spin-nematic quantum qutrits, bridging the gap between theoretical prediction and experimental feasibility.

2. Theoretical Model. We consider a spin-1 BEC confined in a quasi-two-dimensional toroidal trap. In the mean-field framework, the system is described by the spinor order parameter $\Psi(\boldsymbol{r},t)=[\psi_1,\psi_0,\psi_{-1}]^{\mathrm{T}}$. The system's dynamics are governed by the energy functional $\mathcal{E}=\int \mathrm{d}^2\boldsymbol{r}(\mathcal{E}_0+\mathcal{E}_{\mathrm{int}})$. The interaction energy density is given by

$$\mathcal{E}_{\mathrm{int}}=\frac{c_0}{2}n^2+\frac{c_2}{2}|\boldsymbol{F}|^2, \tag{1}$$

where $n=\Psi^\dagger\Psi$ is the total atomic density and $\boldsymbol{F}=\Psi^\dagger\boldsymbol{S}\Psi$ is the spin density vector, where $\boldsymbol{S}=(S_x,S_y,S_z)$ are the spin-1 matrices. The coefficients c_0 and c_2 characterize the density-dependent and spin-dependent interaction strengths, respectively.

The single-particle energy density reads $\mathcal{E}_0=\Psi^\dagger[-\hbar^2\nabla^2/(2m)+V_{\mathrm{ext}}+H_{\mathrm{SOC}}]\Psi$. The external potential V_{ext} is engineered to form a toroidal geometry,[23]

$$V_{\mathrm{ext}}(r)=\frac{1}{2}m\omega_\perp^2 r^2+H\mathrm{e}^{-r^2/w^2}, \tag{2}$$

where m is the atomic mass, $\omega_\perp$ is the radial trapping frequency, and H and w denote the height and width of the central repulsive Gaussian barrier.

The SOC is induced by a pair of co-propagating Laguerre–Gaussian Raman beams, described by the Hamiltonian

$$\begin{aligned}H_{\mathrm{SOC}}=\;&\Omega(r)\left(\mathrm{e}^{-2\mathrm{i}\phi}\psi_1^\dagger\psi_0+\mathrm{e}^{-2\mathrm{i}\phi}\psi_{-1}^\dagger\psi_0+\mathrm{h.c.}\right)\\&+\delta S_z+qS_z^2.\end{aligned} \tag{3}$$

Here, ϕ is the azimuthal angle, δ is the two-photon detuning, S_z is the z-component of the spin-1 matrices, and q represents the quadratic Zeeman shift. The radial coupling profile follows $\Omega(r)=2\Omega_0(r/w_{\mathrm{R}})^2\exp(-2r^2/w_R^2)$, determined by the peak Rabi frequency Ω_0 and the Raman beam waist w_{R}.

To eliminate the phase factor $\exp(-2\mathrm{i}\phi)$, we apply a unitary transformation $\tilde{\Psi}=U^\dagger\Psi$ with $U=\exp(-2\mathrm{i}\phi S_z^2)$. This rotation introduces a synthetic gauge potential $\boldsymbol{A}=-\mathrm{i}\hbar U^\dagger\nabla U$, which shifts the canonical angular momentum of the $m_{\mathrm{F}}=\pm1$ components by $-2\hbar$. Furthermore, the rotation modifies the transverse spin interaction terms, introducing a phase-dependent mixing factor $\exp(\pm4\mathrm{i}\phi)$ in the spin-exchange channel.

Minimizing the energy functional yields the dimensionless coupled Gross–Pitaevskii equations. We rescale length units by the harmonic oscillator length $a_{\mathrm{ho}}=\sqrt{\hbar/m\omega_\perp}$ and energy units by $\hbar\omega_\perp$. The resulting dimensionless equations are[39]

$$\begin{aligned}&\mathrm{i}\frac{\partial\psi_{\pm1}}{\partial t}\\&=\left[\mathcal{L}_\pm+V(r)\mp\delta+q\right]\psi_{\pm1}+\Omega(r)\psi_0\\&\quad+\left[g_nn+g_s(n_{\pm1}+n_0-n_{\mp1})\right]\psi_{\pm1}+g_s\mathrm{e}^{+4\mathrm{i}\phi}\psi_0^2\psi_{\mp1}^*,\\&\mathrm{i}\frac{\partial\psi_0}{\partial t}\\&=\left[\mathcal{L}_0+V(r)\right]\psi_0+\Omega(r)(\psi_1+\psi_{-1})\\&\quad+\left[g_nn+g_s(n_1+n_{-1})\right]\psi_0+2g_s\mathrm{e}^{+4\mathrm{i}\phi}\psi_1\psi_{-1}\psi_0^*,\end{aligned} \tag{4}$$

where $\mathcal{L}_\alpha=-\nabla^2/2+(L_z-\alpha)^2/(2r^2)$ is the gauge-modified kinetic energy operator, with the recoil parameter $\alpha=2$ for the $m_F=\pm1$ components and $\alpha=0$ for the $m_{\mathrm{F}}=0$ component. The dimensionless interaction parameters are given by $g_n=4\pi N(a_0+2a_2)/3$ and $g_s=4\pi N(a_2-a_0)/3$. In the following discussions, all parameters (including H,w,Ω_0) are expressed in these dimensionless units.

To characterize the complex spin textures, we introduce the spin-nematic vector $\boldsymbol{n}$, which is defined within a specific SU(2) subspace embedded in the full SU(3) algebra. This vector is constructed from the transverse spin density and the nematic tensor components as[40]

$$\boldsymbol{n}=\frac{1}{\mathcal{N}}\left(S_x,\,2\mathcal{N}_{yz},\,\mathcal{D}_{yz}\right), \tag{5}$$

where $\mathcal{N}$ is a normalization factor. The spin operators are $\boldsymbol{S}=\{S_x,S_y,S_z\}$, and the symmetrized nematic tensors are defined as $\mathcal{N}_{\mu\nu}=(S_\mu S_\nu+S_\nu S_\mu)/2-2\delta_{\mu\nu}/3$. Using the bare spin basis $|1\rangle,|0\rangle,|-1\rangle$, the specific matrix representations required to construct our subspace $\boldsymbol{n}=\{S_x,2\mathcal{N}_{yz},\mathcal{D}_{yz}\}$ are

$$S_x=\frac{1}{\sqrt{2}}\begin{pmatrix}0&1&0\\1&0&1\\0&1&0\end{pmatrix},\quad \mathcal{N}_{yz}=\frac{\mathrm{i}}{2\sqrt{2}}\begin{pmatrix}0&-1&0\\1&0&1\\0&-1&0\end{pmatrix}. \tag{6}$$

And the component $\mathcal{D}_{yz}$ is given by the difference $\mathcal{N}_{yy}-\mathcal{N}_{zz}$. This vector $\boldsymbol{n}$ serves as the primary order parameter for distinguishing the singular vortex phase (where $\boldsymbol{n}$ implies a texture on the Bloch sphere equator) from the coreless phases.

We distinguish two topological invariants to quantify the system's geometry and topology. The first is the total winding number W, which characterizes the quantized circulation of the global superfluid phase. For a multicomponent spinor $\Psi(\boldsymbol{r})$, the gauge-invariant definition of the winding number along a closed loop $\mathcal{C}$ enclosing the trap center is given by

$$W=\frac{1}{2\pi}\oint_{\mathcal{C}}\mathrm{Im}\left[\frac{\Psi^\dagger\nabla\Psi}{\Psi^\dagger\Psi}\right]\cdot\mathrm{d}\boldsymbol{l}. \tag{7}$$

On a discretized spatial grid, this integral is rigorously evaluated by summing the relative phase differences between adjacent grid points via the overlap product,

$$W=\frac{1}{2\pi}\sum_j\arg\left[\Psi^\dagger(\boldsymbol{r}_j)\Psi(\boldsymbol{r}_{j+1})\right], \tag{8}$$

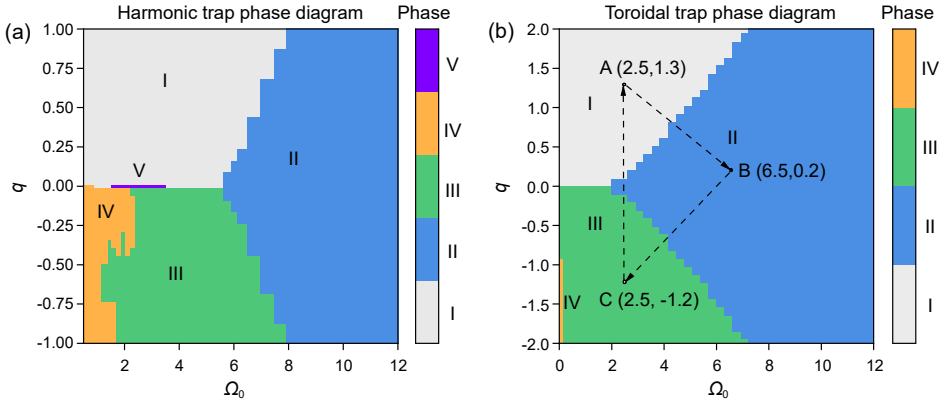

Fig. 1. Ground-state phase diagrams of a spin-1 spin–orbit coupled BEC in the Ω_0–q plane. (a) Results for a harmonic trap potential $V_{\rm ext} = r^2/2$. (b) Results for a toroidal trap with an additional Gaussian plug $V_{\rm plug} = H\exp(-r^2/w^2)$ ($H = 5.0, w = 0.8$). Numerical simulations are performed with interaction strengths $c_0 = 1.0$ and $c_2 = -0.1$. Distinct phases I–V are identified by the total angular momentum $\langle L_z\rangle$ and spin projection $\langle S_z\rangle$.

where $\boldsymbol{r}_j$ denotes the coordinates along the azimuthal path. This integer invariant W directly labels the angular momentum states $|L_z\rangle$ corresponding to $W = 0, 1, 2$.

The second invariant is the Skyrmion charge Q, a continuous geometric index that measures the global coverage of the Bloch sphere by the vector texture $\boldsymbol{n}(\boldsymbol{r})$,

$$Q = \frac{1}{4\pi}\int \mathrm{d}^2\boldsymbol{r}\,\boldsymbol{n}\cdot\left(\frac{\partial \boldsymbol{n}}{\partial x}\times\frac{\partial \boldsymbol{n}}{\partial y}\right). \tag{9}$$

Unlike W, which is strictly quantized to integers due to the single-valuedness of the wavefunction, Q is determined by the specific texture boundaries and can take non-integer values. The decoupling between the discrete topological index W (digital) and the continuous geometric index Q (analog) is a key feature explored in this work.

3. Numerical Results. The ground states of the system are determined by minimizing the Gross–Pitaevskii energy functional via imaginary-time propagation. Unlike standard finite-difference schemes on Cartesian grids, we employ a high-precision spectral Galerkin method in polar coordinates (r, θ). The spinor wave functions $\psi_j(\boldsymbol{r})$ (with $j = 0, \pm 1$) are expanded in a truncated basis of Laguerre–Gaussian modes as

$$\psi_j(r,\theta) = \sum_{n=0}^{N_r}\sum_{m=-M_\theta/2}^{M_\theta/2} c_{n,m}^{(j)}\mathcal{R}_n(r)\mathrm{e}^{\mathrm{i}m\theta}. \tag{10}$$

$\mathcal{R}_n(r)$ are the radial basis functions constructed from generalized Laguerre polynomials,

$$\mathcal{R}_n^\alpha(r) = \sqrt{\frac{2n!}{(n+\alpha)!}}r^\alpha \mathrm{e}^{-r^2/2}L_n^\alpha(r^2), \tag{11}$$

where L_n^α is the generalized Laguerre polynomial, n is the radial quantum number, and α is determined by the absolute value of the angular momentum m. $\exp(\mathrm{i}m\theta)$ capture the angular momentum harmonics. This spectral representation is particularly advantageous for systems with rotational symmetry, allowing for an exact treatment of the kinetic energy operator and the angular momentum transfer induced by the Raman coupling. In our simulations, the basis is truncated at $N_r = 30$ radial modes and $M_\theta = 40$ angular modes, ensuring spectral convergence and accurately resolving the vortex core structure.

4. Phase Diagram. To evaluate the impact of trap geometry, we explore the ground-state phase diagram in the Ω_0–q parameter space. To isolate the geometric effect, all parameters—including the interaction strengths (c_0, c_2), the Raman beam width, and the basis truncation—are fixed between the two geometries. The key geometric parameters are the height of the central Gaussian barrier H and plug width w.

In the harmonic trap limit ($H = 0$), the system exhibits five distinct topological phases distinguished by the expectation value of the orbital angular momentum (OAM) $\langle L_z\rangle$ and spin projection $\langle S_z\rangle$ [Fig. 1(a)]. These include: (I) the Polar phase ($L_z \approx 0$); (II) the singular spin-nematic vortex ($L_z \approx 1$); (III) the double-vortex phase ($L_z \approx 2$); (IV) the ferromagnetic phase ($L_z \approx 2$, $|\langle S_z\rangle| > 0$) with broken spin-parity symmetry; and (V) the angular stripe phase where rotational symmetry is broken (non-integer L_z). In this phase, the expectation value $\langle L_z\rangle$ is not quantized but varies continuously between 0.268 and 0.675 within the parameter range studied. This non-integer value arises because Phase V is a coherent superposition of the $L_z = 0$ and $L_z = 2$ modes, with the expectation value given by $\langle L_z\rangle = 2|D_+|^2$, where $|D_+|^2$ is the fractional population of the $L_z = 2$ component. As the Raman coupling Ω_0 increases from 1.548 to 3.381, $\langle L_z\rangle$ increases monotonically, reflecting a gradual shift in the weight of the constituent angular momentum states.

A notable characteristic of the harmonic geometry is the high critical Raman coupling required to stabilize the singular vortex. For instance, the triple point where phases I, II, and III converge is located at $\Omega_0 \approx 6.0$. Below this threshold, the $L_z = 1$ state remains suppressed due to the high energetic cost of maintaining a phase singularity at the trap's density maximum. This energetic mismatch effectively prevents the formation of a stable vortex core, favoring either Polar or coreless textures instead.

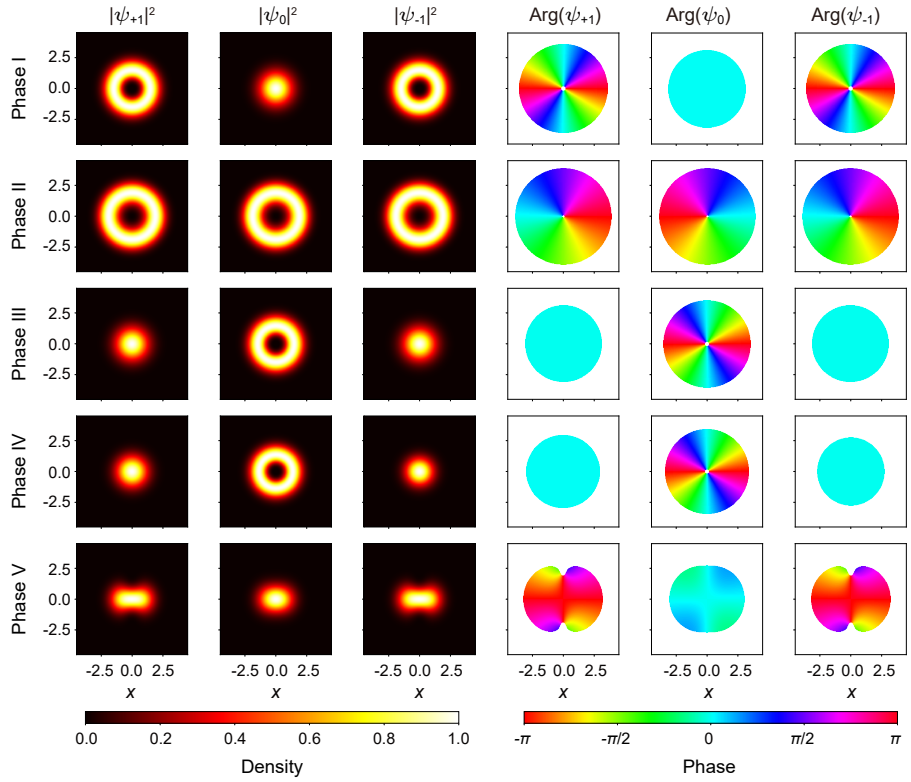

Fig. 2. Density profiles and phase distributions of the spin-1 BEC in the non-transformed lab frame. Left panel: pseudocolor plots of the density distribution $|\psi_i(x,y)|^2$ in each phase, where the 1st, 2nd, and 3rd columns correspond to the density distribution on the bare spin components $+1$, 0, and -1, respectively. Right panel: the corresponding phase distributions of the wave functions in the x–y plane, i.e., $\arg[\psi_i(x,y)]$. In our calculation, we considered an isotropic 2D harmonic confinement and set the interaction parameters to $c_0 = 1$ and $c_2 = -0.1\,c_0$. The specific parameters $\{\Omega_0, q\}$ we take for the five rows (from top to bottom, corresponding to Phase I to Phase V) are: $\{4, 0.5\}$ for Phase I, $\{10, 0\}$ for Phase II, $\{4, -0.5\}$ for Phase III, $\{2, -0.5\}$ for Phase IV, and $\{4, 0\}$ for Phase V.

The implementation of a central Gaussian barrier ($H = 5.0, w = 0.8$) leads to a significant reshaping of the phase boundaries [Fig. 1(b)]. Most notably, the stability regime of the singular vortex (Phase II) expands considerably toward the weak-coupling regime. The triple point, which marks the confluence of phases I, II, and III, shifts leftward to $\Omega_0 \approx 2.3$. This substantial threshold reduction confirms that density depletion at the trap center effectively removes the energetic cost associated with the vortex core. Consequently, the $L_z = 1$ state becomes energetically competitive even at much lower Raman coupling strengths.

Furthermore, the symmetry-broken phases are remarkably sensitive to this geometric modification: Phase V is completely suppressed, while the ferromagnetic Phase IV is compressed into a narrow domain at $q < 0$. In harmonic traps, Phase V arises from the spatial interference between the $L_z = 0$ and $L_z = 2$ modes. However, the central plug modifies the radial density profiles of these modes, reducing their spatial overlap and suppressing the interference terms required to sustain angular stripes. As a result, the toroidal geometry favors pure angular momentum eigenstates, simplifying the phase diagram into robust topological sectors that are ideal for deterministic state preparation.

In our phase diagrams, the ground states are labeled by their quasi-OAM L_z, which serves as a rigorously conserved quantum number in the rotating frame. However, to establish the physical reality of these topological states and confirm that the vortex structures are not merely mathematical artifacts of the unitary transformation, it is crucial to analyze the wavefunctions in the original, non-transformed laboratory frame.

The mapping from the rotating-frame wavefunction $\tilde{\Psi}$ back to the laboratory-frame wavefunction $\Psi_{\rm lab}$ is given by the inverse unitary transformation $\Psi_{\rm lab} = \exp(-2i\phi S_z^2)\tilde{\Psi}$. Physically, this transformation reintroduces the explicit spatial phase factors imparted by the Laguerre–Gaussian Raman beams, reflecting the actual transfer of OAM to the atoms. Consequently, the bare spin components acquire distinct mechanical OAMs in the laboratory frame: the $m_{\rm F} = 0$ component carries a mechanical OAM of L_z, while both the $m_{\rm F} = +1$ and $m_{\rm F} = -1$ components carry $L_z - 2$.

To visualize these physical consequences, we plot the laboratory-frame density profiles and phase distributions for the distinct phases in Fig. 2. For our target state—the singular spin-nematic vortex (Phase II, $L_z = 1$)—the laboratory-frame mapping yields a mechanical OAM of $+1$ for the $m_{\rm F} = 0$ component, and $1 - 2 = -1$ for the $m_{\rm F} = \pm 1$ components. As shown in the second row of Fig. 2, the corresponding phase distributions $\arg(\psi_{0,\pm1})$ perfectly exhibit these ± 1 quantized phase windings. Because every bare spin component carries a non-zero me-

chanical circulation, the physical density of the entire condensate must strictly vanish at the trap center ($r = 0$). This density-depleted core is a frame-independent, physical observable, definitively confirming that Phase II is a genuine singular vortex driven by the Raman optical fields.

By contrast, the ground states in Phase I ($L_z = 0$) and Phase III ($L_z = 2$) manifest as coreless vortices. As depicted in the first and third rows of Fig. 2, Phase I features zero mechanical OAM in the $m_{\rm F} = 0$ component, while Phase III features zero mechanical OAM in the $m_{\rm F} = \pm 1$ components. Since at least one spin component lacks vorticity in these states, the total density remains finite at the trap core. The symmetry-broken phases exhibit further distinct structural signatures: the ferromagnetic Phase IV inherits the coreless nature of Phase III but shows asymmetric populations in the $m_{\rm F} = \pm 1$ components due to spin-parity symmetry breaking. Finally, Phase V displays angular stripe patterns resulting from the spatial interference of components with different mechanical OAMs, visually confirming the rotational symmetry breaking in the laboratory frame.

5. Tunable Metastability and Hysteresis. For a topological state to be useful in quantum information processing, such as a quantum memory or a qutrit, it must be robust against parameter fluctuations. Knowing the static phase diagram is insufficient; we must determine whether the intermediate singular vortex state ($L_z = 1$) can survive dynamically when parameters are swept.

To characterize the robustness of the system, the hysteresis loop is numerically calculated by adiabatically sweeping the Raman coupling strength Ω_0. The expectation value of the angular momentum $\langle L_z \rangle$ is tracked during both the forward (from 0 to 10) and backward (from 10 to 0) sweeps to monitor the stability of the topological state.

The competition between the toroidal geometry and the Raman coupling generates distinct metastable behaviors, as shown in Fig. 3. For a moderate barrier height [$H = 5.0$, Fig. 3(a)], the system exhibits a broad, rewritable hysteresis window. During the forward sweep, the system remains in the Polar phase ($\langle L_z \rangle \approx 0$) until a high threshold $\Omega_{c1} \approx 4.2$. However, during the backward sweep, the topological state ($\langle L_z \rangle \approx 1$) is protected by a local energy barrier and survives down to a much lower threshold $\Omega_{c2} \approx 0.8$. This bistability functions as a rewritable quantum memory: the topological state can be written, robustly retained, and subsequently erased by fully turning off the Raman lasers.

In the strong confinement regime [$H = 20.0$, Fig. 3(b)], the dynamics shift qualitatively toward irreversible topological locking. While the forward transition occurs at a reduced threshold ($\Omega_{c1} \approx 3.0$), the backward sweep reveals that the system remains locked in the $\langle L_z \rangle = 1$ state even as $\Omega_0 \to 0$. This indicates that the central potential barrier imposes a global geometric constraint that prevents vortex unwinding, effectively functioning as a permanent "write-once" switch.

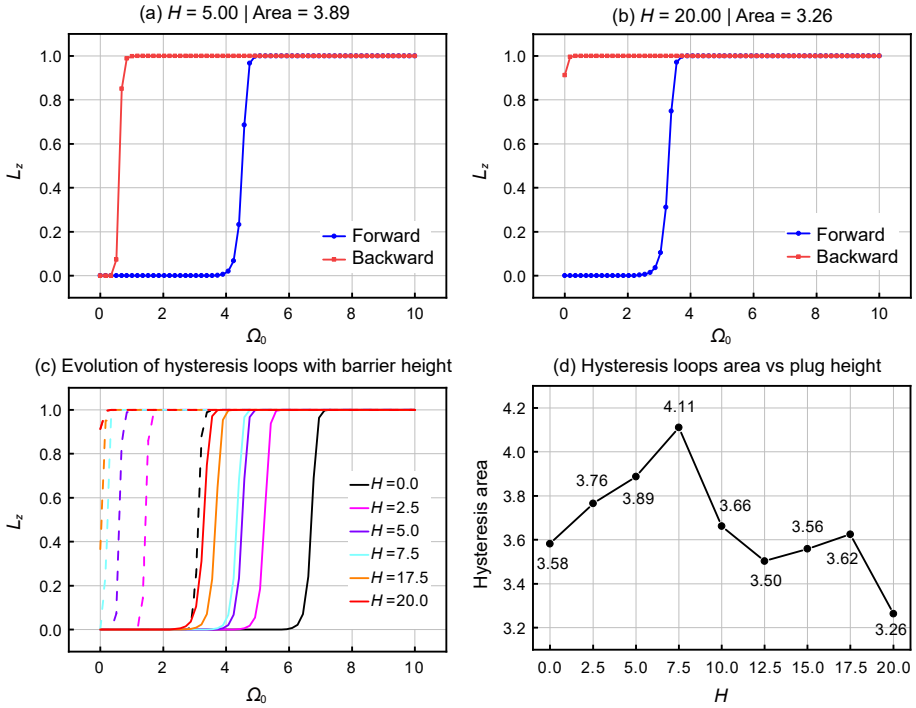

Fig. 3. Hysteresis loops and topological stability dependence on the barrier height H. Angular momentum $\langle L_z \rangle$ is recorded during forward (blue, $0 \to 10$) and backward (red, $10 \to 0$) adiabatic sweeps of Ω_0. (a) Bidirectional hysteresis at $H = 5.0$. (b) Irreversible topological locking at $H = 20.0$, where the $L_z = 1$ state remains stable at $\Omega_0 = 0$. (c) Evolution of the critical Raman coupling thresholds as a function of H. Solid curve denotes the turn-on threshold Ω_{c1} (forward transition), while the dot curve denotes the turn-off threshold Ω_{c2} (backward transition). The vanishing of Ω_{c2} for $H \gtrsim 15$ signifies the transition to the irreversible regime. (d) Integrated hysteresis area $A = \int (\langle L_z \rangle_{\rm back} - \langle L_z \rangle_{\rm fwd}) {\rm d}\Omega_0$ versus H, revealing a non-monotonic optimization of topological protection. All calculations use fixed $w = 0.8$ and $q = 0.2$.

The evolution of these boundaries is summarized in Fig. 3(c). The turn-on threshold (Ω_{c1}) decreases monotonically from ~ 6.2 in the harmonic limit to ~ 3.0 at $H = 20$, confirming that removing the core singularity substantially lowers the energy cost for vortex formation. For $H \geq 15$, the turn-off threshold (Ω_{c2}) vanishes, signifying the transition from a reversible switch to the irreversible locking mode.

To quantify topological stability, we calculate the hysteresis loop area, $A = \int (\langle L_z \rangle_{\rm back} - \langle L_z \rangle_{\rm fwd}) {\rm d}\Omega_0$. As shown in Fig. 3(d), this area displays a non-monotonic dependence on H, driven by two competing mechanisms. The initial rise ($H = 0 \to 7.5$) reflects the optimization of core removal: eliminating the energetic cost of the vortex core deepens the local minimum of the $L_z = 1$ state, broadening the metastability window.

However, as the ring expands further ($H \approx 10 \sim 20$), the loop area contracts. This contraction arises because the forward threshold Ω_{c1} drops rapidly. Although the backward path remains maximally stable (locked at $\Omega_{c2} = 0$), the reduced width of the bistable region ($\propto \Omega_{c1}$) limits the total integrated area compared to the intermediate regime.

Consequently, the barrier height H serves as a versatile control knob. Tuning H to the hysteresis maximum ($H \approx 7.5$) maximizes robustness against noise, ideal for memory applications. Conversely, the high-barrier regime ($H \geq 15$) minimizes the initialization threshold by sacrificing reversibility, enabling low-power deterministic preparation of the topological qutrit.

6. Deterministic Topological Pumping. The deterministic preparation of specific topological states is a cornerstone of quantum simulation and topological quantum computing. In SOC BECs, while the static phase diagram supports exotic states like the singular spin-nematic vortex ($L_z = 1$), their dynamic realization via parameter sweeps remains a non-trivial challenge. A fundamental obstacle is the high energetic cost associated with the density-depleted core of a vortex, which must compete with the trap's tendency to maximize density at its center. In standard harmonic traps, this geometric incompatibility often results in a "dynamic bypass". During an adiabatic sweep, the system may undergo a discontinuous transition, jumping directly from a polar phase to a double-vortex phase ($L_z : 0 \to 2$). This uncontrolled leap effectively bypasses the target $L_z = 1$ state, severely limiting the precision of topological state engineering.

We propose that such dynamical instabilities are not intrinsic to the Hamiltonian itself, but rather products of the trapping geometry. By transforming the trap from a harmonic to a toroidal profile, we introduce a central repulsive barrier that naturally matches the vortex core. To demonstrate the efficacy of this geometric intervention, the real-time dynamics are numerically simulated under a closed triangular parameter sweep: $A(2.5, 1.3) \to B(6.5, 0.2) \to C(2.5, -1.2) \to A$. Throughout this evolution, four critical observables are tracked (Fig. 4): the quasi-OAM $\langle L_z \rangle$, the quantized winding number W, the continuous Skyrmion charge Q, and the structural annularity parameter A. To verify the robustness of the process under realistic conditions, a 3% stochastic noise is incorporated into the Hamiltonian. The total evolution time for each pumping stage is $T \approx 131$ (in units of $\omega_\perp^{-1}$), which is significantly larger than the characteristic trap period (~ 6.3). This ensures that the system remains in the instantaneous ground state throughout the process.

The results reveal that the toroidal geometry restores a clean, stepwise adiabatic evolution [Figs. 4(a) and 4(b)]. We fix the toroidal barrier height at $H = 5.0$ and vary the plug width w (from 0.4 to 1.4), comparing these results against the standard harmonic trap limit ($H = 0$). The evolution of the angular momentum $\langle L_z \rangle$ and the winding number W reveals that successful topological state preparation depends critically on the precise tuning of the trap geometry.

In the harmonic trap (dashed red lines), the intermediate state is dynamically inaccessible. The system remains arrested in the Polar phase ($\langle L_z \rangle \approx 0$) for the majority of the A→B leg, before undergoing a direct, discontinuous transition to the $L_z \approx 2$ state. This confirms that without geometric engineering, the singular vortex state ($L_z = 1$) is dynamically unstable and effectively bypassed.

For toroidal potentials, simply introducing a barrier is insufficient; the geometry must be optimized. As shown in Figs. 4(a) and 4(b), optimal performance is achieved at a plug width of $w = 0.8$ (solid green lines). In this regime, the system exhibits a deterministic, stepwise transition $0 \to 1 \to 2$. The winding number W locks onto the integer plateau $W = 1$ over a broad temporal window, demonstrating a robust topological pump.

While the winding number W exhibits discrete quantization ("Digital Topology"), the Skyrmion charge Q [Fig. 4(c)] displays a continuous, smooth evolution ("Analog Geometry"). Notably, within the stable window where $W = 1$ is locked (for optimal $w = 0.8$), Q varies continuously. This decoupling arises because W is topologically protected by the single-valuedness of the wavefunction phase, whereas Q depends on the detailed geometric texture of the spin vector $\boldsymbol{n}$ on the Bloch sphere. This dual behavior suggests that the toroidal system can simultaneously serve as a robust quantum memory (protected by W) and a sensitive geometric sensor (readout via Q).

The physical mechanism underlying this stabilization is quantified by the "annularity" parameter, $A = (\rho_{\rm max} - \rho_{\rm center})/\rho_{\rm max}$. The harmonic trap maintains low annularity until the sudden formation of the vortex. In contrast, toroidal potentials enforce high annularity ($A \to 1$) from the outset, confining the condensate into a rigid ring structure.

Crucially, the degree of this geometric confinement dictates the stability of the pumping process. Wider plugs (e.g., $w = 1.4$, dark blue lines) sustain a "stiffer" ring geometry ($A \approx 1$), which correlates with the widest $W = 1$ plateaus. However, in this strong confinement regime, the geometric stiffness is so robust that it inhibits the subsequent transition to the $L_z = 2$ phase, keeping the system

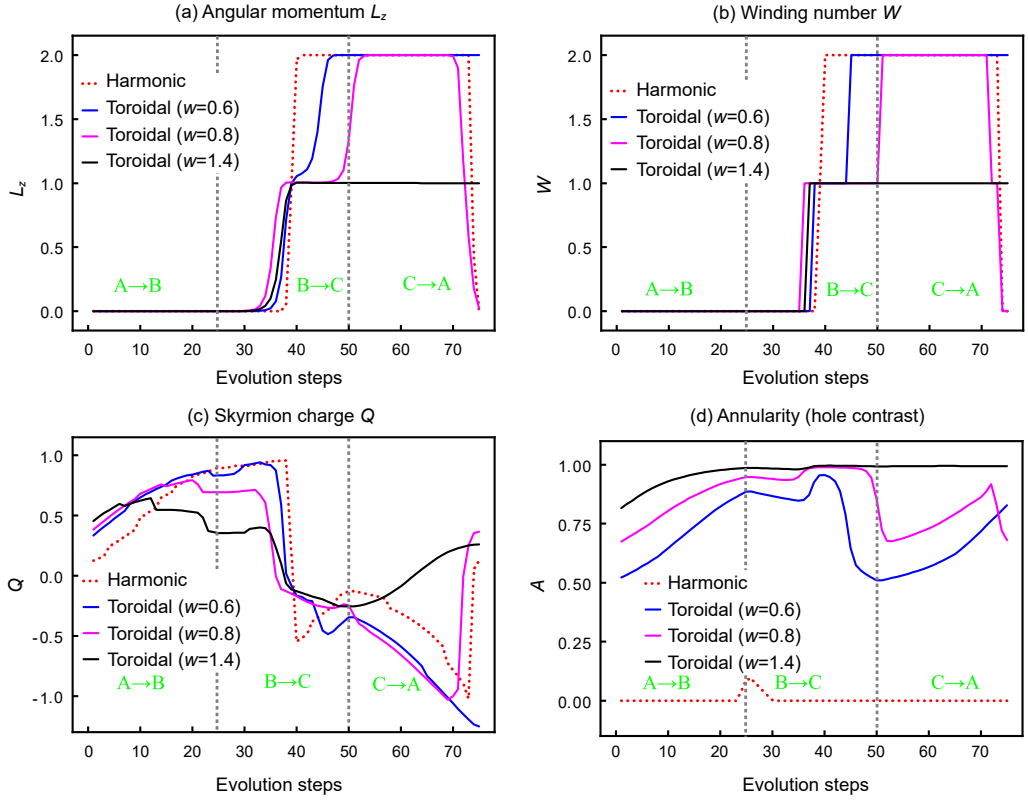

Fig. 4. Topological pumping dynamics and geometric characterization. The system is driven along a cyclic parameter path $\mathrm{A}(2.5, 1.3) \to \mathrm{B}(6.5, 0.2) \to \mathrm{C}(2.5, -1.2) \to \mathrm{A}$. (a) Evolution of the angular momentum $\langle L_z \rangle$. (b) Winding number W, defined by the phase accumulation $\Delta\phi/2\pi$ around the trap center. (c) Skyrmion charge $Q = (1/4\pi)\int \boldsymbol{n}\cdot(\partial_x \boldsymbol{n} \times \partial_y \boldsymbol{n})\mathrm{d}x\mathrm{d}y$, representing the local spin texture. (d) Annularity parameter $A = [\rho_{\max} - \rho(0)]/\rho_{\max}$, quantifying the suppression of central density. Solid lines denote toroidal trap results with varying plug widths $w_p \in [0.4, 1.4]$ at fixed height $H = 5.0$. Dashed red lines indicate the harmonic trap benchmark ($H = 0$). A stochastic noise of amplitude $\eta = 0.03$ is applied to verify topological robustness.

locked in the singular vortex state. This contrasts with the optimal case ($w = 0.8$), which strikes a balance—providing sufficient stiffness to stabilize $L_z = 1$ while remaining flexible enough to permit the transition to $L_z = 2$ at higher couplings.

7. Conclusion. In summary, we have shown that toroidal traps effectively solve the instability problem of singular spin-nematic vortices. The ring geometry naturally matches the density-depleted core, removing the high energy cost found in harmonic traps. This setup lowers the formation threshold by about 50%, which significantly reduces heating from the Raman lasers. Furthermore, the ring potential recovers deterministic dynamics: instead of the random jumps seen in harmonic traps, it supports a clean, step-by-step evolution ($|L_z = 0\rangle \to |1\rangle \to |2\rangle$). Our results demonstrate that simple geometry control is a powerful tool for realizing high-fidelity spin-nematic quantum qutrits.

Acknowledgements. This work was supported by the National Natural Science Foundation of China (Grant Nos. 12547184, 12033007, 12103058, 12203058, and 12074309). We thank Professor Xiao-Fei Zhang for valuable discussions.

References

[1] Lin Y J, Jiménez-García K, and Spielman I B 2011 *Nature* **471** 83
[2] Galitski V and Spielman I B 2013 *Nature* **494** 49
[3] Wang P, Yu Z Q, Fu Z, Miao J, Huang L, Chai S, Zhai H, and Zhang J 2012 *Phys. Rev. Lett.* **109** 095301
[4] Cheuk L W, Sommer A T, Hadzibabic Z, Yefsah T, Bakr W S, and Zwierlein M W 2012 *Phys. Rev. Lett.* **109** 095302
[5] Wang Y, Cui J L, Zhang H K, Zhao Y, Xu S L, and Zhou Q 2024 *Chin. Phys. Lett.* **41** 090302
[6] Zhang L, Zhang L, Niu Q, and Liu X J 2018 *Phys. Rev. Lett.* **120** 106401
[7] Aidelsburger M, Nascimbene S, and Goldman N 2018 *C. R. Phys.* **19** 394
[8] Zhang X F, Wen L, Dai C Q, Zhang R F, Wong D E, and Liu W M 2015 *Phys. Rev. A* **91** 023610
[9] Zhang X F, Han W, Jiang H F, Liu W M, and Zhang S G 2014 *Phys. Rev. A* **90** 043622
[10] Amico L, Boshier M, Birkl G *et al.* 2021 *AVS Quantum Sci.* **3** 039201
[11] Wright K C, Blakestad R B, Lobb C J, Phillips W D, and Campbell G K 2013 *Phys. Rev. Lett.* **110** 025302
[12] Ho T L 1998 *Phys. Rev. Lett.* **81** 742
[13] Ohmi T and Machida K 1998 *J. Phys. Soc. Jpn.* **67** 1822
[14] Li J R, Lee J, Huang W, Burchesky S, Shteynas B, Top F, Jamison A O, and Ketterle W 2017 *Nature* **543** 91
[15] Léonard J, Morales A, Zupancic P, Esslinger T, and Donner T 2017 *Nature* **543** 87

[16] Chomaz L, Ferrier-Barbut I, Ferlaino F *et al.* 2023 *Rep. Prog. Phys.* **86** 026401
[17] Xiao T N, Yao D Y, Zhang C, Fan Z J, and Deng Y J 2025 *Chin. Phys. Lett.* **42** 070002
[18] Ueda M 2014 *Rep. Prog. Phys.* **77** 122401
[19] Kawaguchi Y and Ueda M 2012 *Phys. Rep.* **520** 253
[20] Lovegrove J, Borgh M O, and Ruostekoski J 2012 *Phys. Rev. A* **86** 013613
[21] Choi J, Kang S, Seo S W, Kwon W J, and Shin Y 2012 *Phys. Rev. Lett.* **108** 045302
[22] Qiu X, Hu A Y, Cai Y Y, Saito H, Zhang X F, and Wen L 2023 *Phys. Rev. A* **107** 033308
[23] Zhang X F, Kato M, Han W, Zhang S G, and Saito H 2017 *Phys. Rev. A* **95** 033620
[24] da Silva B P, Marques B A D, Rodrigues R B, Ribeiro P H S, and Khoury A Z 2021 *Phys. Rev. A* **103** 063704
[25] Nayak C, Simon S H, Stern A, Freedman M, and Das Sarma S 2008 *Rev. Mod. Phys.* **80** 1083
[26] Zhu S L, Fu L B, Wu C J, Zhang S C, and Duan L M 2006 *Phys. Rev. Lett.* **97** 240401
[27] Ho T L and Zhang S 2011 *Phys. Rev. Lett.* **107** 150403
[28] Li Y, Martone G I, Pitaevskii L P, and Stringari S 2013 *Phys. Rev. Lett.* **110** 235302
[29] Sánchez-Baena J, Boronat J, and Mazzanti F 2020 *Phys. Rev. A* **101** 043602
[30] Khamehchi M A, Zhang Y, Hamner C, Busch T, and Engels P 2014 *Phys. Rev. A* **90** 063624
[31] Ji S C, Zhang L, Xu X T, Wu Z, Deng Y, Chen S, and Pan J W 2015 *Phys. Rev. Lett.* **114** 105301
[32] Fetter A L 2009 *Rev. Mod. Phys.* **81** 647
[33] Prataviera G A, Zapata J, and Meystre P 2000 *Phys. Rev. A* **62** 023605
[34] Campbell D L, Price R M, Putra A, Valdés-Curiel A, Trypogeorgos D, and Spielman I B 2016 *Nat. Commun.* **7** 10897
[35] Li Y, Pitaevskii L P, and Stringari S 2012 *Phys. Rev. Lett.* **108** 225301
[36] Zhang J Y, Ji S C, Chen Z *et al.* 2012 *Phys. Rev. Lett.* **109** 115301
[37] Ryu C, Andersen M F, Cladé P, Natarajan V, Helmerson K, and Phillips W D 2007 *Phys. Rev. Lett.* **99** 260401
[38] Ramanathan A, Wright K C, Muniz S R, Zelan M, Hill W T, Lobb C J, Helmerson K, Phillips W D, and Campbell G K 2011 *Phys. Rev. Lett.* **106** 130401
[39] Lan Z Z 2024 *Chin. Phys. Lett.* **41** 090501
[40] Chen L, Zhang Y, and Pu H 2020 *Phys. Rev. Lett.* **125** 195303